Energetics of Eddy-Mean Flow Interactions in the East Australian Current System

Junde Li [a] and Moninya Roughan[a]

[a] *School of Biological, Earth and Environmental Sciences, University of New South Wales, Sydney, NSW, 2052, Australia*

Corresponding author: Junde Li, junde.li@unsw.edu.au

1

ABSTRACT: Examining eddy-mean flow interactions in western boundary currents (WBCs) is crucial for understanding the mechanisms of mesoscale eddy generation and the role of eddies in the large-scale circulation. However, this analysis is lacking in the East Australian Current (EAC) system. Here we show the detailed three-dimensional structure of the eddy-mean flow interactions and energy budget in the EAC system. The energy reservoirs and conversions are greatest in the upper 500 m, with complex vertical structures. Strong mean kinetic energy is confined within a narrow band (24.5°S-32.5°S) in the EAC jet. Most energy is contained in the eddy fields instead of the mean flow in the EAC typical separation and extension regions (south of 32.5°S). Strong barotropic instability is the primary source of eddy kinetic energy north of 36°S, while baroclinic instability dominates the eddy kinetic energy production in the EAC southern extension, which peaks in the subsurface. The mean flow transfers 5.22 GW of kinetic energy and 3.33 GW of available potential energy to the eddy field in the EAC typical separation region. The largest conversion term is from available potential energy conversion from the mean flow to the eddy field through baroclinic instability, dominating between 29°S-35.5°S. Nonlocal eddy-mean flow interactions also play a role in the energy exchange between the mean flow and the eddy fields. This study provides the mean state of the eddy-mean flow interactions in the EAC system, paving the way for further studies exploring seasonal and interannual variability and provides a baseline for assessing the impact of environmental change.

1. Introduction

Western boundary currents (WBCs) are the western branch of the subtropical ocean gyres, which are swift, narrow and energetic flows (Hu et al. 2015). The WBC extensions are among the most eddy-rich regions of the global ocean, showing a significant increase in mesoscale eddy activity of 2–5% per decade (Martínez-Moreno et al. 2021). The WBCs and eddies can exchange energy, vorticity and momentum through eddy-mean flow interactions, influencing the local large-scale circulation and eddy activity (Chen et al. 2014). The transfer of energy from the mean flow to eddies through barotropic, baroclinic and mixed instability processes leads to eddy formation and shedding (Macdonald et al. 2016; Vallis 2017). In turn, the energy transferred from the eddies back to the mean flow through rectification and topographic steering processes (Mata et al. 2006; Kuo and Chern 2011; Witter and Chelton 1998) can feed the mean flow. A quantitative description of the oceanic energy cycle among different energy reservoirs is of critical importance for improving our understanding of the ocean general circulation and dynamical process of a current system (Storch et al. 2012), particularly in the eddy-rich WBC regions.

The East Australian Current (EAC) is the WBC of the South Pacific subtropical gyre and flows southward along the east coast of Australia, with strong kinetic energy in the core of the EAC jet (Storch et al. 2012; Feng et al. 2016; Sloyan et al. 2016; Bull et al. 2018; Li et al. 2021). After the EAC separates from the coast (Godfrey et al. 1980), typically at around 31°S-33°S (Cetina-Heredia et al. 2014), it bifurcates into two branches (Tilburg et al. 2001): the EAC eastern extension and the EAC southern extension (Oke et al. 2019a,b), and anticyclonic eddies shed from the main jet (Nilsson and Cresswell 1980; Marchesiello and Middleton 2000; Oke and Middleton 2000). The EAC eastern extension flows eastward towards New Zealand, and the EAC southern extension continues to flow southward towards Tasmania (Ridgway and Dunn 2003). It has been shown that the EAC can separate at any latitude along its path (Cetina-Heredia et al. 2014; Kerry and Roughan 2020; Li et al. 2022b), forming an energetic mesoscale eddy field (Everett et al. 2012), with the highest eddy kinetic energy (EKE) occurring between 33.1°S and 36.6°S (Li et al. 2021).

To investigate the eddy shedding process in the EAC, previous studies examined the energy conversion terms from mean available potential energy (MPE) to eddy available potential energy (EPE) through baroclinic instabilities and from mean kinetic energy (MKE) to EKE through barotropic instabilities (Bowen et al. 2005; Mata et al. 2006; Bull et al. 2017). These earlier studies

3

were based on model output with coarse horizontal resolution (>20 km), which is insufficient to resolve the mesoscale process, hence they show different dynamical mechanisms. For example, Bowen et al. (2005) proposed that anticyclonic eddies shed from the EAC jet mainly due to the barotropic instability of the mean flow, but Mata et al. (2006) and Bull et al. (2017) suggested that the generation of eddies is characterized by mixed barotropic and baroclinic instabilities, with barotropic energy conversion being dominant. Recently, based on a long-term (22-year), high-resolution (2.5-6 km) model simulation, Li et al. (2021) demonstrated that the barotropic instability is the primary source of EKE and the decay of cyclonic eddies can convert EKE back into MKE in some regions (~27°S-28°S and ~30.5°S-31.5°S). Previous studies mainly focus on the sources of EKE, however, little is known about the eddy-mean flow interactions in the EAC system.

Energetics analysis is an effective method for investigating the eddy–mean flow interaction by quantifying the energy exchange between the time-mean large-scale circulation and time-varying mesoscale flows. It has been widely used to study the eddy-mean flow interactions among the major WBCs of the global ocean, such as in the Gulf Stream (Kang and Curchitser 2015) (hereafter referred to as KC15), the Kuroshio Current (Yang and Liang 2016, 2018; Yan et al. 2019, 2022), the Brazil Current (Magalhães et al. 2017; Brum et al. 2017) and Agulhas Current (Halo et al. 2014; Tedesco et al. 2022). These studies systematically investigated the energetics evolution of four of the five major WBCs and their associated eddies. However, unlike the other four WBCs, the quantitative three-dimensional description of the energy exchange between the EAC and mesoscale eddy reservoirs has never been investigated in the EAC system.

The objective of this study is to present the first detailed investigation into the three-dimensional structure of the eddy-mean flow interactions and energy budget in the EAC system. We perform the energetics analysis based on a 24-year (1998-2021) high-resolution (0.1° × 0.1°) reanalysis and examine four energy reservoirs (MKE, EKE, MPE and EPE) and the energy conversion terms among them. We conduct our analysis in three key regions identified for their dynamical regimes: the EAC jet, the typical EAC separation region and the EAC southern extension. This paper is structured as follows: section 2 provides the theoretical framework; section 3 describes the observations and the numerical model simulation; section 4 presents the detailed analysis of eddy-mean flow interactions; the main findings are summarized and discussed in section 5.

2. Diagnostic framework

a. Governing equations

Following the framework of KC15, the derivation of the governing equations is based on the Reynolds-averaged Navier–Stokes equations using the hydrostatic and Boussinesq approximations, along with the continuity and scalar transport equations, which can be written as:

$$\frac{\partial u}{\partial t} + \mathbf{u} \cdot \nabla u - fv = -\frac{1}{\rho_0}\frac{\partial p}{\partial x} + \mathcal{F}_u + \mathcal{D}_u \tag{1}$$

$$\frac{\partial v}{\partial t} + \mathbf{u} \cdot \nabla v + fu = -\frac{1}{\rho_0}\frac{\partial p}{\partial y} + \mathcal{F}_v + \mathcal{D}_v \tag{2}$$

$$\frac{\partial C}{\partial t} + \mathbf{u} \cdot \nabla C = \mathcal{F}_C + \mathcal{D}_C \tag{3}$$

$$\frac{\partial p}{\partial z} = -\rho g \tag{4}$$

$$\nabla \cdot \mathbf{u} = 0 \tag{5}$$

where $\mathbf{u} = (u, v, w)$ is the velocity vector, f is the Coriolis frequency, $\rho_0 = 1025$ kg m^{-3} is the constant part of the density ρ, p is the pressure, g is the gravitational acceleration, and $\mathcal{F}$ and $\mathcal{D}$ represent the forcing and horizontal diffusive terms, respectively. Here C can be temperature T and salinity S, then the density can be calculated from the equation of state $\rho = \rho(T, S, Z)$, which is given by:

$$\rho(x, y, z, t) = \rho_r(z) + \rho_a(x, y, z, t) \tag{6}$$

where ρ_r is a predefined reference density. It is chosen to be the area average of the time-mean density that is a constant at a given depth, and ρ_a is the perturbation density. Following Storch et al. (2012), we can derive the density transport from the temperature T and salinity S transport in Eq. (3) and the equation of state. Applying the density decomposition Eq. (6) yields

$$\frac{\partial \rho_a}{\partial t} + \mathbf{u} \cdot \nabla \rho_a = \frac{\rho_0 N^2}{g} w + \mathcal{F}_{\rho_a} + \mathcal{D}_{\rho_a} \tag{7}$$

5

where the buoyancy frequency N is defined by

$$N^2 \equiv -\left(\frac{g}{\rho_0}\right)\frac{d\rho_r}{dz} \tag{8}$$

b. Energy definitions

To obtain the mean flow and eddy energy equations, all the time-varying variables are decomposed as $\Phi(x,y,z,t) = \overline{\Phi(x,y,z)} + \Phi'(x,y,z,t)$. Here overbar and prime denote the time-mean and the deviation from the time mean, and Φ can be u, v, w, p and ρ.

MKE and EKE are defined as

$$\text{MKE} = \frac{1}{2}\rho_0(\overline{u}^2 + \overline{v}^2) \tag{9}$$

$$\text{EKE} = \frac{1}{2}\rho_0\overline{(u'^2 + v'^2)} \tag{10}$$

MPE and EPE are defined as

$$\text{MPE} = \frac{g^2\overline{\rho_a}^2}{2\rho_0 N^2} \tag{11}$$

$$\text{EPE} = \frac{g^2\overline{\rho_a'^2}}{2\rho_0 N^2} \tag{12}$$

Applying the variable decomposition to the perturbation density ρ_a, we find

$$\rho_a' = (\rho - \rho_r) - \overline{(\rho - \rho_r)} = \rho - \overline{\rho} = \rho' \tag{13}$$

therefore, ρ_a' is independent of the reference density ρ_r.

c. Energy budget equations

The MKE budget equation with its sources, sinks and energy conversion terms can be derived by multiplying the momentum equations Eq. (1) and (2) by $\rho_0\overline{u}$ and $\rho_0\overline{v}$, respectively, then taking the time average of their sum. Similarly, the EKE budget equation can be derived by multiplying the momentum equations Eq. (1) and (2) by $\rho_0 u'$ and $\rho_0 v'$, respectively, then taking the time average of their sum.

6

The MPE budget equation can be obtained by multiplying the density transport equation Eq. (7) by $g^2\overline{\rho_a}/\rho_0 N^2$, then taking the time average. Similarly, the EPE budget equation can be obtained by multiplying the density transport equation Eq. (7) by $g^2\overline{\rho_a'}/\rho_0 N^2$, then taking the time average.

The energy budget equations for MKE, EKE, MPE and EPE are defined as:

$$\underbrace{\frac{\partial \mathrm{MKE}}{\partial t}}_{\text{unsteadiness}} = \underbrace{-g\overline{\rho_a}\;\overline{w}}_{\mathrm{PmKm}} + \underbrace{\rho_0(\overline{u'\mathbf{u}'}\cdot\nabla\overline{u} + \overline{v'\mathbf{u}'}\cdot\nabla\overline{v})}_{-\mathrm{KmKe}}$$

$$\underbrace{-\rho_0\nabla\cdot\overline{\mathbf{u}'(\overline{u}u' + \overline{v}v')}}_{\mathrm{NLKE}}$$

$$\underbrace{-\nabla\cdot(\overline{\mathbf{u}}\;\overline{p_a})}_{\mathrm{PW}} \underbrace{-\nabla\cdot(\overline{\mathbf{u}}\mathrm{MKE})}_{\mathrm{DF_k}}$$

$$+\underbrace{\rho_0\overline{\mathbf{u}}_H\cdot\overline{\mathcal{F}_H}}_{\mathrm{F_k}} + \underbrace{\rho_0\overline{\mathbf{u}}_H\cdot\overline{\mathcal{D}_H}}_{\mathrm{D_k}} \qquad (14)$$

$$\underbrace{\frac{\partial \mathrm{EKE}}{\partial t}}_{\text{unsteadiness}} = \underbrace{-g\overline{\rho_a'w'}}_{\mathrm{PeKe}} \underbrace{-\rho_0(\overline{u'\mathbf{u}'}\cdot\nabla\overline{u} + \overline{v'\mathbf{u}'}\cdot\nabla\overline{v})}_{\mathrm{KmKe}}$$

$$\underbrace{-\nabla\cdot(\overline{\mathbf{u}'p'})}_{\mathrm{PW'}} \underbrace{-\nabla\cdot(\overline{\mathbf{u}\mathrm{EKE}})}_{\mathrm{DF_k'}} \qquad (15)$$

$$+\underbrace{\rho_0\overline{\mathbf{u}_H'\cdot\mathcal{F}_H'}}_{\mathrm{F_k'}} + \underbrace{\rho_0\overline{\mathbf{u}_H'\cdot\mathcal{D}_H}'}_{\mathrm{D_k'}}$$

$$\underbrace{\frac{\partial \mathrm{MPE}}{\partial t}}_{\text{unsteadiness}} = \underbrace{g\overline{\rho_a}\;\overline{w}}_{-\mathrm{PmKm}} + \underbrace{\frac{g^2}{\rho_0 N^2}\overline{\mathbf{u}'\rho_a'}\cdot\nabla\overline{\rho_a}}_{-\mathrm{PmPe}}$$

$$\underbrace{-\frac{g^2}{\rho_0 N^2}\nabla\cdot\overline{\mathbf{u}'\rho_a'}\overline{\rho_a}}_{\mathrm{NLPE}}$$

$$\underbrace{-\nabla\cdot(\overline{\mathbf{u}}\mathrm{MPE})}_{\mathrm{DF_p}} + \underbrace{\frac{g^2}{\rho_0 N^2}\overline{\rho_a}\overline{\mathcal{F}_\rho}}_{\mathrm{F_\rho}} + \underbrace{\frac{g^2}{\rho_0 N^2}\overline{\rho_a}\overline{\mathcal{D}_\rho}}_{\mathrm{D_\rho}} \qquad (16)$$

7

$$\underbrace{\frac{\partial \text{EPE}}{\partial t}}_{\text{unsteadiness}} = \underbrace{g\overline{\rho'_a w'}}_{-\text{PeKe}} \underbrace{- \frac{g^2}{\rho_0 N^2}\overline{\mathbf{u}'\rho'_a}\cdot\nabla\overline{\rho_a}}_{\text{PmPe}}$$

$$\underbrace{- \nabla\cdot(\overline{\mathbf{u}\text{EPE}})}_{\text{DF}'_\text{p}} + \underbrace{\frac{g^2}{\rho_0 N^2}\overline{\rho'_a \mathcal{F}'_\rho}}_{\text{F}'_\rho} + \underbrace{\frac{g^2}{\rho_0 N^2}\overline{\rho'_a \mathcal{D}'_\rho}}_{\text{D}'_\rho} \tag{17}$$

where $\mathbf{u}_H$ is the horizontal velocity vector. p_a and p' are the reference pressure and perturbation pressure that are related to ρ_a and ρ', respectively. The unsteadiness terms on the left-hand side (LHS) of Eqs. (14)-(17) denote the temporal change rates of MKE, EKE, MPE and EPE, respectively. On the right-hand side (RHS), the last terms PW, DF, F and D represent the energy redistribution rates through pressure work, advection, forcing effects and turbulent diffusivity, respectively. The energy exchanges between the mean flow and the eddy fields among different energy reservoirs and the oceanic external energy have been illustrated in KC15 and Yan et al. (2019). In this study, the atmospheric forcing and dissipation terms are not explicitly evaluated because we focus on the eddy–mean flow interaction terms as listed in Table 1.

The definitions of local and non-local eddy-mean flow interactions were introduced by Chen et al. (2014) and discussed in Chen et al. (2016) and Yan et al. (2019). The non-local eddy-mean flow interaction terms NLKE and NLPE are shown to connect the MKE and MPE with the external ocean energy, where NLKE (NLPE) represents the energy conversion of EKE↔MKE (EPE↔MPE) (Chen et al. 2016; Yan et al. 2019). KC15 considered these terms as the mean energy flux divergences of the cross kinetic energy (NLKE) and available potential energy (NLPE). If the volume integrals of the divergence forms (NLKE and NLPE) are negligible, the eddy–mean flow interaction is called local because almost all the energy released from the mean flow is converted to eddy energy in the same region. For a fixed non-closed ocean region, their magnitudes are not negligible, hence part of the energy released from the mean flow is conveyed outside of the domain instead of being used to sustain the local eddy energy growth in the same region.

8

TABLE 1. The eddy–mean flow interaction terms used in this study.

Term	Mathematical form	Interpretation
KmKe	$-\rho_0\left(\overline{u'\mathbf{u}'}\cdot\nabla\overline{u}+\overline{v'\mathbf{u}'}\cdot\nabla\overline{v}\right)$	MKE→EKE conversion rate due to eddy momentum flux
PeKe	$-g\overline{\rho_a'w'}$	EPE→EKE conversion rate due to vertical eddy density flux
PmKm	$-g\overline{\rho_a}\,\overline{w}$	MPE→MKE conversion rate due to vertical mean density flux
PmPe	$-\dfrac{g^2}{\rho_0 N^2}\overline{\mathbf{u}'\rho_a'}\cdot\nabla\overline{\rho_a}$	MPE→EPE conversion rate due to horizontal eddy density fluxes
NLKE	$-\rho_0\nabla\cdot\overline{\mathbf{u}'(\overline{u}u'+\overline{v}v')}$	EKE→MKE kinetic energy conversion rate due to nonlocal eddy-mean flow interactions
NLPE	$-\dfrac{g^2}{\rho_0 N^2}\nabla\cdot\overline{\mathbf{u}'\rho_a'}\overline{\rho_a}$	EPE→MPE potential energy conversion rate due to nonlocal eddy-mean flow interactions

3. Data and methods

a. Satellite observations

Satellite observations, including absolute geostrophic current velocity and geostrophic current velocity anomalies, are obtained from Archiving, Validation and Interpretation of Satellite Oceanographic (AVISO) (Ducet et al. 2000), which are distributed by the Copernicus Marine and Environment Monitoring Service (https://marine.copernicus.eu/). Here we use AVISO+ daily data, which has a horizontal resolution of $0.25° \times 0.25°$ and spans from January 1998 to December 2021.

b. Model data and validation

To investigate the three-dimensional energetics structure of the eddy-mean flow interactions in the EAC, in this study, we use the daily output from BRAN2020 (Chamberlain et al. 2021). BRAN2020 is an ocean reanalysis that combines observations with an eddy-resolving, near-global ocean general circulation model, which is the latest version of the Bluelink ReANalysis. BRAN2020 has a horizontal resolution of $0.1° \times 0.1°$ and 51 vertical layers, with a 5 m vertical resolution down to 40 m and a 10 m vertical resolution to 200 m. The model output is a realistic reconstruction of mesoscale upper ocean dynamics around Australia (Chamberlain et al. 2021). Based on BRAN2020, we calculate energy reservoirs and energy conversion terms over the period of 1998-2021.

To illustrate the performance of BRAN2020 in representing the EAC and associated mesoscale eddy fields, we show the spatial distributions of surface MKE and EKE from BRAN2020 and AVISO observations. The EAC forms at approximately 15°S in the South Coral Sea and flows poleward along Australia's southeast coast. The main core of the EAC originates at around ~24.5°S
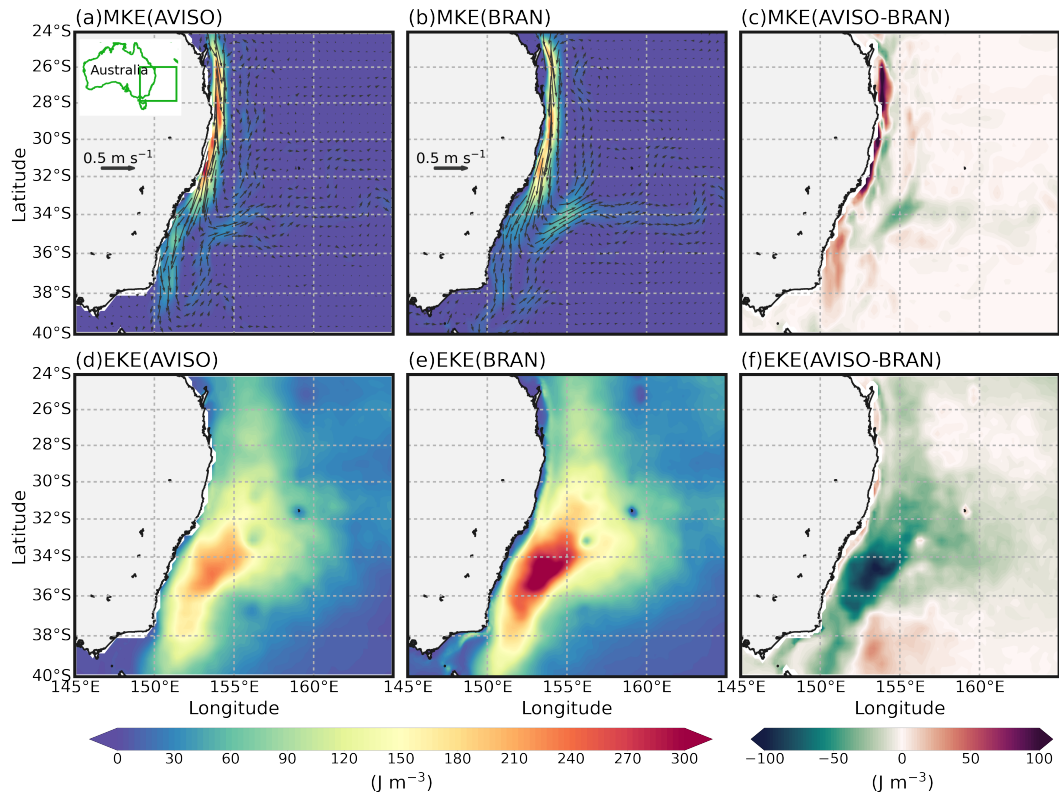
9

FIG. 1. Spatial distribution of surface MKE from (a) AVISO observations and (b) BRAN2020 over the 24 years (1998-2021). The dark gray vectors in panels (a) and (b) indicate surface geostrophic velocities. (c) Differences of surface MKE between AVISO observations and BRAN2020. (d)-(f), as (a)-(c), but for the EKE.

and separates from the coast at ~32.5°S (Figs. 1a-b), with one branch flowing eastward and the other continuing to flow southward. Although the surface MKE along the EAC path in BRAN2020 is weaker than the AVISO observations (Fig. 1c), the locations and separation latitudes of the EAC jet in BRAN2020 are consistent with that in the AVISO observations. The spatial distributions of BRAN2020 surface EKE also agree well with the AVISO observations (Figs. 1d-e), with the highest surface EKE in the EAC typical separation region (32.5°S-35.8°S) where anticyclonic eddies shed from the main jet. However, the BRAN2020 surface EKE is stronger than the AVISO observations in most regions (Fig. 1f), particularly in the EAC typical separation region and the EAC southern extension. We suspect this is a result of the increased resolution in BRAN2020 compared to AVISO.

We acknowledge that there may be uncertainties in the BRAN2020 fields introduced through the data assimilation process. To quantify the impact on our calculations, we also calculated the

10

energy reservoirs and energy conversion terms from a free-running model output Ocean Forecasting Australian Model version 2017 (OFAM2017), which has no data assimilation (Oke et al. 2013). This model uses the same free running ocean model as BRAN2020, but covers a shorter period (1994-2016) and has data assimilation. These results are presented and compared below (e.g. Fig. 2).

c. Energy calculations

It is noted that the energy terms MPE, EPE and three related energy conversion terms PmKm, PmPe and NLPE depend on the choice of reference stratification. By examining the sensitivity of energy analysis results to different ρ_r profiles, KC15 found that EPE and PmPe are slightly affected by the choice of ρ_r because of their similar structures and fairly constant volume-integrated values. Following KC15 and Yan et al. (2019), in this study, we choose ρ_r as the horizontal average over the whole EAC region (24°S-40°S, 145°E-165°E) in Fig. 2 for the entire 24-year simulation period. We then evaluate the four energy terms (MKE, EKE, MPE and EPE), as well as six eddy-mean flow interaction terms (KmKe, PmKm, NLKE, PmPe, PeKe, NLPE) as shown in Table 1. The detailed horizontal and vertical distribution of these terms in the EAC system are presented in the following section.

d. Key dynamical regions

Here we focus on three key regions along the EAC path identified using dynamical reasoning: the EAC jet region (red box in Fig. 2a, hereafter referred to as EAC jet), the EAC typical separation region (purple box in Fig. 2a, hereafter referred to as EAC eddy) and the EAC southern extension region (orange box in Fig. 2a, hereafter referred to as EAC southern extension). The EAC eddy region is located within the EAC typical separation region, with a similar range of latitudes to those in Oke et al. (2019b) and Li et al. (2021), which encompasses the region of the highest EKE in the EAC system. North of the EAC eddy region, the EAC jet region captures the core of the EAC jet, with a focus on the variability of the mean flow upstream. South of the EAC eddy region, the EAC southern extension region covers both the southward flow of the EAC southern extension and eddy activity south of the EAC typical separation region. We did not explore the EAC eastern extension

11

as identified by Oke et al. (2019a) here, however the variability in this region could form the basis for future work.

4. Results

a. Energy reservoirs

As shown in previous studies (Kerry and Roughan 2020; Li et al. 2021), large EKE is confined within the upper 450 m. A depth of 1000 m has been chosen to study the eddy-mean flow interactions in the other WBC regions, such as in the Gulf Stream (KC15), the Kuroshio Current (Yang and Liang 2016; Yan et al. 2019) and the Brazil Current (Brum et al. 2017), here we choose the 1000 m depth to capture the main dynamics of the eddy-mean flow interactions in the EAC system. We first examine the spatial distributions of the energy reservoirs in the three key dynamics regions from BRAN2020. Figure 2 shows the depth-integrated energy terms (MKE, EKE and EPE) over the upper 1000 m. Along the EAC path, the energy terms exhibit nonuniform distribution. In the EAC jet, strong MKE is confined within a narrow band along the shelf edge from 24.5°S to 32.5°S (Fig. 2a). The EAC separates from the coast at around 32.5°S and bifurcates into the eastward and southward flows. The MKE decreases rapidly south of the separation latitude. In addition, we can also find relatively weak MKE in the EAC eastern extension.

In the EAC separation region, the EKE is the highest and much greater than the MKE in the EAC jet, implying that the EAC jet sheds eddies when it separates from the coast around these latitudes (Fig. 2b). This high EKE region is consistent with a previous study from a higher resolution regional model simulation (Li et al. 2021). The EKE decreases sharply in the EAC southern extension. Upstream of 32.5°S, the EKE is the weakest along the EAC path. This structure of EKE has also been shown in previous studies (Feng et al. 2016; Kerry and Roughan 2020; Li et al. 2021). The horizontal distribution of depth-integrated EPE in the study region is similar to that of EKE, but with a smaller magnitude (Fig. 2c). Compared to BRAN2020, the free-running model OFAM2017 has a much stronger MKE in the EAC jet (Fig. 2d) but weaker EKE (Fig. 2e) and EPE (Fig. 2f) in the EAC system. However, the horizontal distributions of energy reservoirs have very similar patterns in these two model outputs (Fig. 2).

The horizontal distributions of MKE, EKE and EPE at three reference depths (50 m, 200 m and 500 m) are similar to that integrated over the upper 1000 m (Figs. 2, 3) but decrease in magnitude
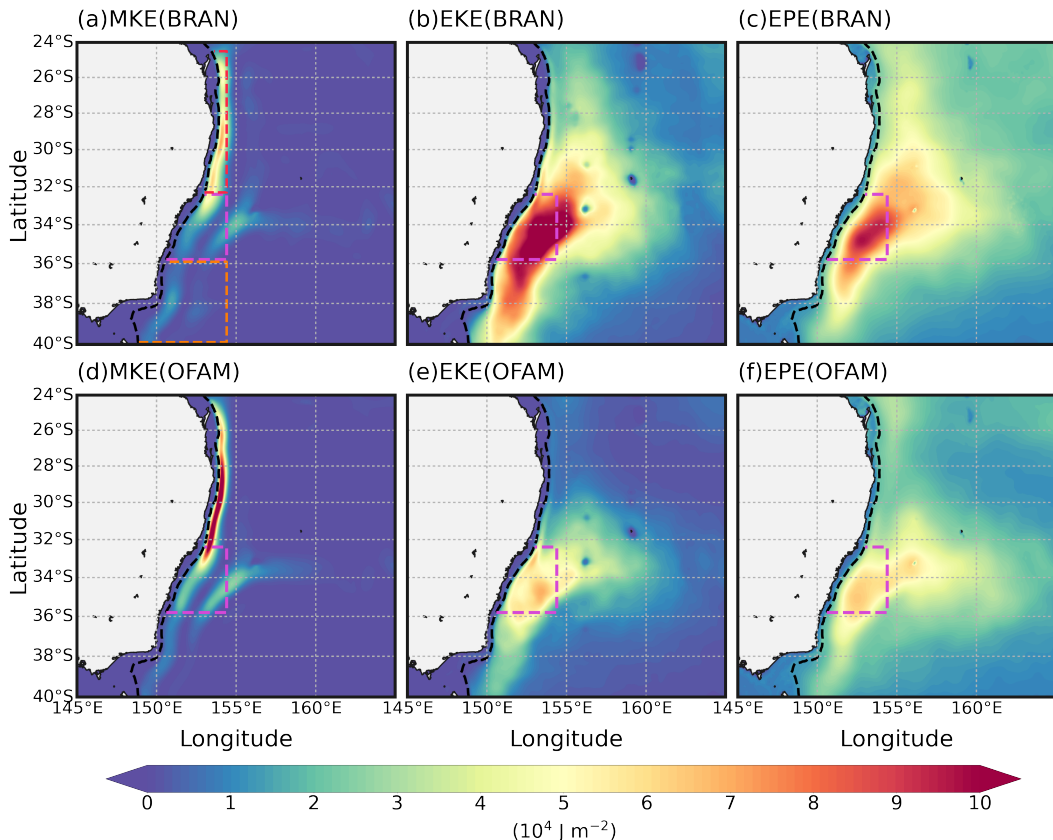
12

Fɪɢ. 2. Horizontal distribution of the depth-integrated (a) MKE, (b) EKE and (c) EPE over the upper 1000 m. The dashed black lines indicate the 200 m isobath. Three labelled boxes in panel (a) represent the focused subdomains in this study: the EAC jet (red), the EAC eddy (purple) and the EAC southern extension (orange). The bottom panels (d)-(f), as (a)-(c), but for the OFAM2017 model.

with depth. These energy terms are the strongest at the surface (50 m), where we can find strong MKE and EPE but weak EKE in the EAC jet region (Figs. 3a-c). In the EAC eddy and EAC southern extension region, the EKE is much larger than MKE and EPE. At 200 m, MKE, EKE and EPE become weaker, but we can still see large EKE and EPE in the EAC eddy region (Figs. 3d-f). At 500 m, these energy terms decrease dramatically and are smaller than 50 J m^{-3}, 80 J m^{-3} and 70 J m^{-3} in the EAC jet, the EAC eddy and the EAC southern extension region (Figs. 3g-i), respectively.

To examine the vertical distributions of the energy reservoirs, we calculate the profiles of energy reservoirs in the EAC jet, eddy and southern extension regions from the surface to 1000 m. In the EAC jet region, although there is a small bump within the pycnocline at around 150 - 200 m
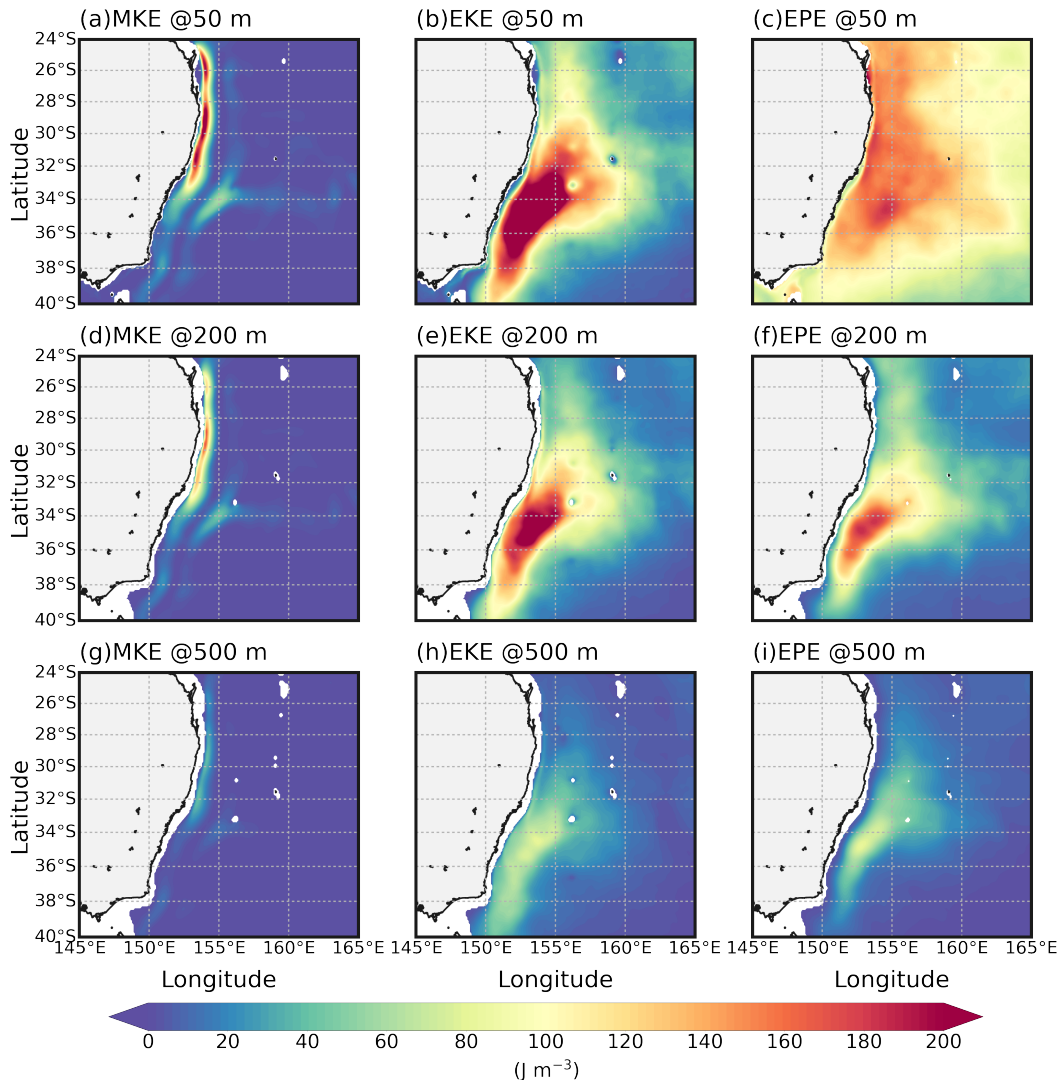
13

FIG. 3. Horizontal distribution of the (a) MKE, (b) EKE and (c) EPE at 50 m. The middle panels (d)-(f), as (a)-(c), but for 200 m. The bottom panels (g)-(f), as (a)-(c), but for 1000 m.

in EPE, all energy reservoirs decrease with depth (Fig. 4a). Compared to the kinetic energy, the available potential energy is larger in the surface but smaller in the deep layer. Above the 286 m, the MPE is the strongest term, but below this depth, it is then much smaller than the other terms. We find strong surface EPE within the upper 65 m, which is larger than MKE and EKE. As the mean flow dominates this region, we find stronger MKE than EKE in the top 325 m. However, the EKE is larger than all the other terms below 325 m.
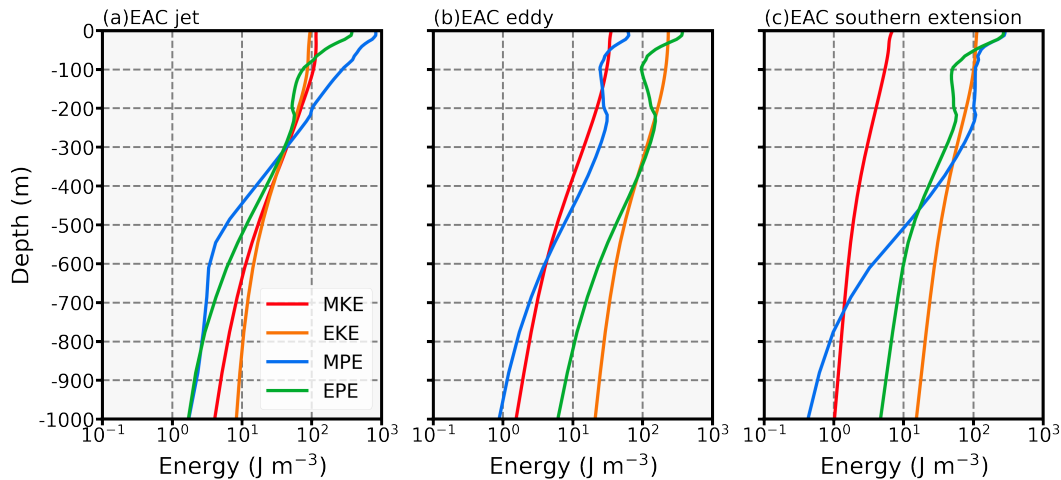
14

FIG. 4. Vertical distribution of the area-mean energy reservoirs averaged over the (a) EAC jet, (b) EAC eddy and (c) EAC southern extension regions indicated in Fig. 2a.

Eddies dominate the EAC eddy region, as shown in Fig. 4b, where the EKE and EPE are much larger than the MKE and MPE, implying that most energy is stored within the eddy field. Both MKE and EKE decrease with depth gradually, but the MPE and EPE have two peaks: one located in the surface and the other is at the 230 m, which is similar to the vertical structures in the Kuroshio Current (Yan et al. 2019) and Gulf of Mexico (Maslo et al. 2020). Both MPE and EPE have a minimum at around 100 m. In the top 30 m, the EPE is the largest, but the EKE is much larger than the other terms below the 500 m.

In the EAC southern extension region, the MKE and EKE also decrease with depth gradually, with EKE larger than MKE over the whole profile (Fig. 4c). Among the four energy terms, the MKE is the weakest above 700 m. The MPE is larger than the other terms above 325 m. In the eddy field, EPE is larger than EKE above 56 m, but is much smaller than EKE below this depth. We also find a minimum of EPE at around 100 m.

To illustrate the meridional distribution of energy terms through the water column, we show the vertical profile of the zonal-mean MKE, EKE and EPE averaged between the 200 m isobath and 154.5°E along the EAC path (Fig. 5). In the EAC jet region, the MKE has two peaks within the upper 200 m (Fig. 5a). The first peak is between 25°S and 26.5°S, and the second one is between 28°S and 30.5°S. The surface MKE decreases as the EAC flows poleward, with a value less than
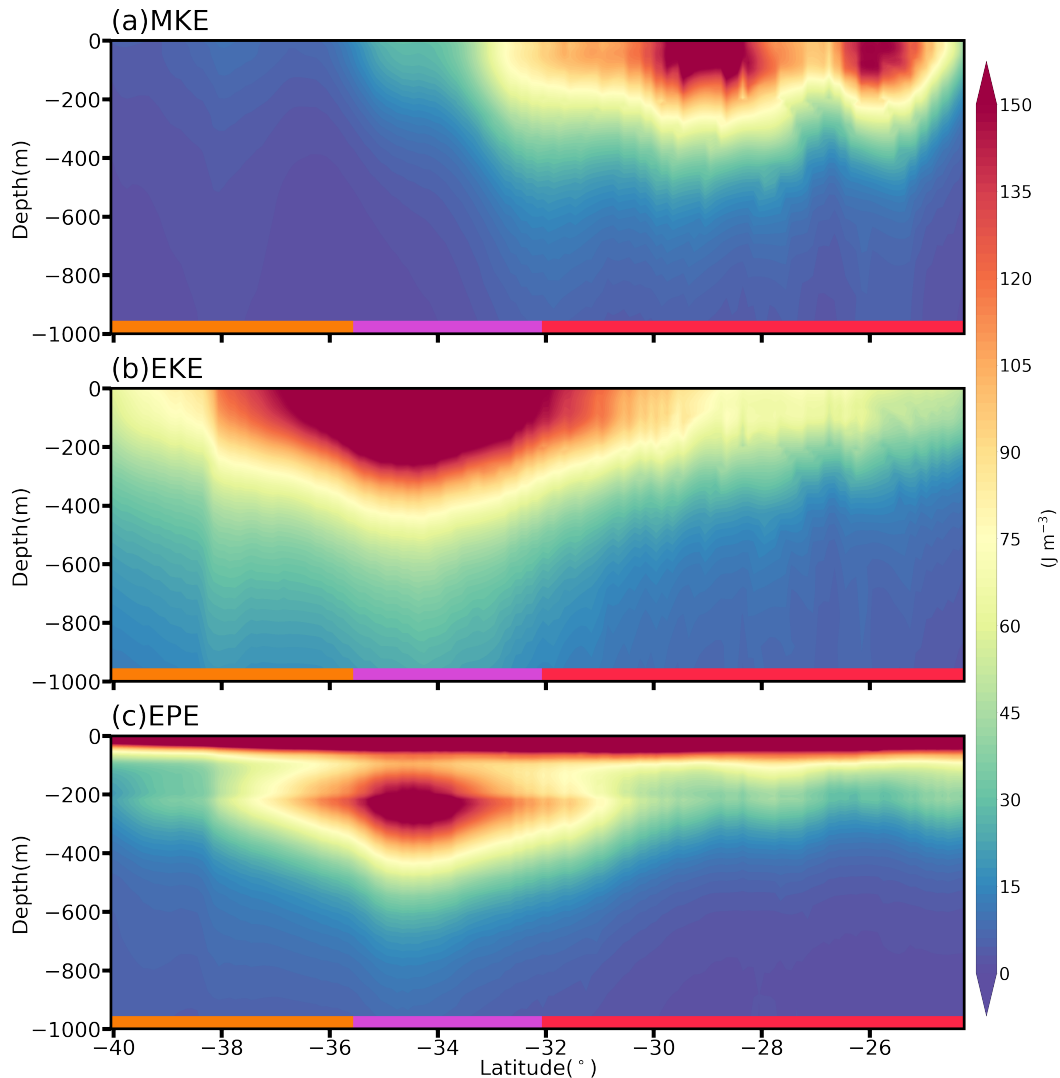
15

FIG. 5. Vertical profile (0-1000 m) of the zonal-mean (a) MKE, (b) EKE and (c) EPE averaged between the 200 m isobath and 154.5°E along the EAC path. The thick red, purple and orange lines on the bottom of each panel indicate the EAC jet, EAC eddy and EAC southern extension regions, respectively.

50 J m^{-3} south of 33°S. The strong MKE in the top layer is consistent with previous observations from a mooring array at 27°S from 2012 to 2013 (Sloyan et al. 2016).

The strongest EKE dominates the EAC eddy regions over the upper 325 m and extends through the EAC separation region from 32°S to 37 °S (Fig. 5b). North of 32°S, the EKE becomes weaker in the EAC jet region. Strong EPE is confined within a shallow layer (< 75 m) along the whole EAC path (Fig. 5c). In addition, we also find strong EPE in the subsurface layer (155 m - 325 m)

16

in the EAC eddy region, consistent with the double peaks structure of the area mean vertical EPE profile in this region in Fig. 4b.

b. Energy conversions

In this section, we examine the energy conversions among the four energy reservoirs. We first show spatial distributions of the depth-integrated energy conversion terms (KmKe, PeKe, NLKE, NLPE, PmKm and PmPe) over the upper 1000 m (Fig. 6). Along the EAC path, we find two strong narrow positive KmKe bands, with one located between 29.5°S and 30.5°S and the other is between 32°S and 33.5°S (Fig. 6a). Positive KmKe indicates that eddies can drain kinetic energy from the mean flow to drive a shedding event, particularly in the EAC eddy region. It is worth noting that we also find two small regions with negative KmKe values, implying an inverse energy cascade from EKE to MKE (Yan et al. 2019). The first is located north of 26°S, and the other is between 27°S and 28.5°S.

Regions of negative KmKe are regions of eddy decay (Gula et al. 2015), which indicates eddies return kinetic energy and momentum to the mean flow. In contrast, the energy conversion from EPE to EKE (PeKe) through baroclinic instability (Fig. 6b) is much weaker than that from MKE to EKE (KmKe) through barotropic instability, implying that the barotropic instability is the main source of EKE in the EAC system. Negative PeKe can also be found in the EAC return flow region (154.5°E-156°E, 33°S-34°S), suggesting that eddies convert EKE to EPE around this region. These horizontal patterns of KmKe and PeKe are consistent with previous studies from higher resolution model simulations (Li et al. 2021, 2022b) who investigated extreme events.

The energy conversion from MPE to MKE (PmKm) is weak in the majority of the EAC system (Fig. 6c) except north of 26°S, but the energy conversion from MPE to EPE (PmPe) is strong along the EAC path (Fig. 6d), consistent with results from high-resolution global ocean models (Storch et al. 2012; Chen et al. 2014). This indicates that most energy stored in MPE is converted to EPE instead of MKE. The strongest PmPe is between 29°S and 35.5°S, where the baroclinic instability facilitates the available potential energy transfer from the mean flow to the eddy field. This spatial distribution of PmPe is also consistent with a previous study (Bull et al. 2017) and is linked to the baroclinic instability of the Tasman Sea (Sloyan and O'Kane 2015). As described in KC15, Magalhães et al. (2017) and Yan et al. (2019), there are two pathways for eddies to draw
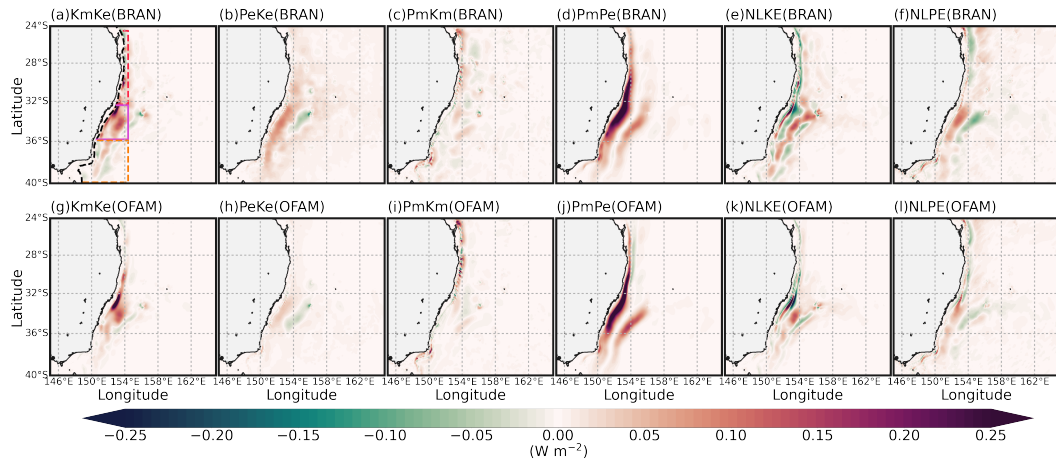
17

FIG. 6. Horizontal distribution of the depth-integrated (a) KmKe, (b) PeKe, (c) PmKm, (d) PmPe, (e) NLKE and (f) NLPE over the upper 1000 m. Three labelled boxes in panel (a) are the same as those in Fig. 2a, which represent the EAC jet (red), the EAC eddy (purple) and the EAC southern extension (orange). The bottom panels (g)-(l), as (a)-(f), but for the OFAM2017 model.

kinetic energy from the mean flow: MKE→EKE and MPE→EPE→EKE. The KmKe term directly transfers MKE to EKE through barotropic instability. PmPe and PeKe provide an indirect route of EKE conversion through baroclinic instability.

Through nonlocal eddy-mean flow interactions, there are two energy conversion pathways for the energy to be transferred from the eddy field to the mean flow: EKE→MKE and EPE→MPE. The NLKE term suggests that part of the MKE converted from (to) the local EKE is transported to (from) eddies in other regions (Yan et al. 2019). The NLPE also represents the nonlocal eddy-mean flow interactions but for the available potential energy. As shown in a global modeling study (Chen et al. 2014), we also find negative NLKE along the EAC path from 24°S to 36°S (Fig. 6e), indicating that nonlocal energy conversion from MKE to EKE. There also exist two positive NLKE bands south of 32°S, where nonlocal eddy-mean flow interactions contribute to the energy conversion from EKE to MKE. The first narrow positive NLKE band is located inshore of the negative NLKE band, and the second one is in the EAC return flow region. For the NLPE pattern, we only find strong nonlocal available potential energy conversion in the EAC upstream (north of 27°S) and the EAC eddy region (Fig. 6f). Compared to BRAN2020, similar horizontal distribution of energy conversion terms are found in the free-running model OFAM2017 (Figs. 6g-l), but with smaller magnitude in most regions.
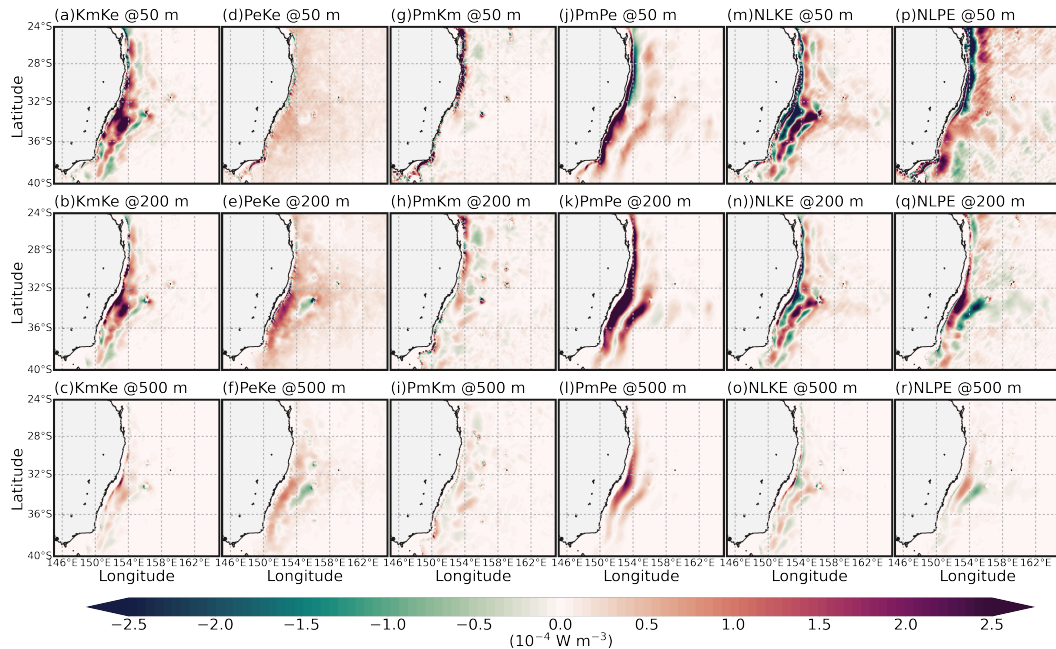
18

FIG. 7. Horizontal distribution of the (a) KmKe, (d) PeKe, (g) PmKm, (j) PmPe, (m) NLKE and (p) NLPE at the 50 m. The middle panels, as the top panels, but for the 200 m. The bottom panels, as the top panels, but for the 500 m.

In the vertical, the kinetic energy conversions (KmKe and NLKE) between the mean flow and the eddy field (MKE↔EKE) keep the same horizontal structure with their strength decreasing from the surface to 500 m (Figs. 7a-c, m-o). PmKm also has similar spatial distribution with strong energy conversions north of $32°$S, and its magnitude decreases with depth from 50 m to 500 m (Figs. 7g-i). Although PeKe has a similar horizontal pattern at 50 m, 200 m and 500 m, its strength peaks at 200 m (Figs. 7d-f).

The horizontal distributions of available potential energy conversions (PmPe and NLPE) between the mean flow and the eddy field (MPE↔EPE) vary with depths (Figs. 7j-l, p-r), which is also consistent with the results in the Gulf Stream (KC15) and Kuroshio Current (Yan et al. 2019). At 50 m, we can find positive PmPe along the EAC path, with a very narrow strip near the shelf in the EAC upstream (Fig. 7j). East of this narrow strip, large negative PmPe is observed between $24°$S and $32°$S, implying that the eddies return available potential energy to the mean flow in this region. At the 200 m and 500 m, positive PmPe is confined within two narrow strips along the EAC path and the path of the EAC return flow (Figs. 7k-l). The strongest energy conversion from MPE to

19

EPE through baroclinic instability can be found in the EAC eddy region at 200 m. NLPE exhibits a positive-negative band structure between 24°S and 33°S at 50 m, but positive NLPE dominates the region south of 33°S (Fig. 7p). However, at the depths of 200 m and 500 m, we can only find strong NLPE in the EAC typical separation region, with positive values near the shelf and negative values in the EAC return flow (Figs. 7q,r).
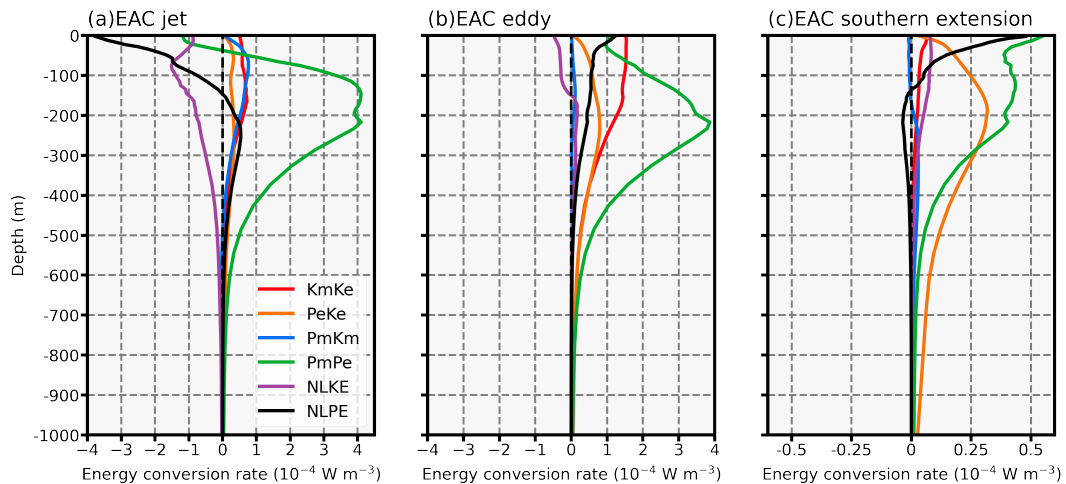

FIG. 8. Vertical distribution of the area-mean energy conversion terms averaged over the (a) EAC jet, (b) EAC eddy and (c) EAC southern extension regions indicated in Fig. 2a. Note the x-axis range in panel (c) is different from that in panels (a) and (b).

To better understand the energy conversions in the three subdomains, we further examine the vertical structure of the six energy conversion terms in the upper 1000 m. In the EAC jet region (Fig. 8a), the energy conversion occurs within the upper 600 m. The KmKe and PeKe are positive through the whole profile, indicating the energy source of EKE through barotropic instability (MKE→EKE) and baroclinic instability (EPE→EKE) (Fig. 8a). We can also find positive PmKm (MPE→MKE) within the upper 550 m, with a peak at 75 m. The PmPe shows the largest energy conversion from MPE to EPE between 125 m and 255 m, with a maximum value of $\sim 4 \times 10^{-4}$ W m^{-3}. However, in the top 40 m, it is negative, indicating an inverse energy conversion from EPE to MPE. For the nonlocal eddy-mean flow energy conversion terms, negative NLKE in the upper 1000 m suggests an energy conversion of MKE→EKE through nonlocal eddy-mean flow interactions. In contrast, the strong negative NLPE only dominates the upper 150 m, with positive values below. This suggests that the available potential energy transfers from the mean flow to the eddy field in

the upper layer (0-150 m) through nonlocal eddy-mean flow interactions, but there is an inverse energy conversion of EPE→MPE below 150 m due to nonlocal eddy-mean flow interactions.

In the EAC eddy region (Fig. 8b), all the energy conversion terms are positive within the upper 550 m except NLKE, which is negative in the upper 150 m, implying that nonlocal eddy-mean flow interactions contribute to the energy conversion from MKE to EKE in this region. Compared to the KmKe and PeKe in the EAC jet region, these two terms are much stronger here. In addition, the KmKe is about two times larger than PeKe in the upper 285 m, suggesting that barotropic instability is the main source of EKE in the EAC eddy region. This result is consistent with a previous study from a regional high-resolution (free-running) simulation (Li et al. 2021). PmKm is the weakest energy conversion term over the whole profile, and strong positive PmPe dominates the energy conversion with a peak at ~220 m. This suggests that the mean flow releases most available potential energy to the eddy field through baroclinic instability. Nonlocal eddy-mean flow interactions contribute to the inverse energy conversion of EPE→MPE, which decreases with depth and extends deeper to around 400 m.

Energy conversion terms in the EAC southern extension region (Fig. 8c) are on average an order of magnitude smaller than in the other two regions. However, relatively, energy conversion related to EPE (PeKe, PmPe and NLPE) dominates the EAC southern extension region (Fig. 8c). Compared to KmKe which is weak positive and decreases with depth, PeKe is stronger over the whole profile, implying that (although weak) baroclinic instability is the main source of EKE in the EAC southern extension region. Similar to that in the EAC eddy region, PmKm is also very weak in the EAC southern extension, particularly in the top 150 m, suggesting no energy conversions between MPE and MKE. Most available potential energy is converted from mean flow to the eddy field, as shown in the dominant PmPe over the upper 600 m. Positive NLKE in the upper 400 m shows that eddies from other regions transfer EKE to MKE in the EAC southern extension. In contrast, most nonlocal inverse available potential energy conversion of EPE→MPE is confined within the upper 140 m, but with negative NLPE below this layer.

To further examine the vertical energy conversion structures along the EAC path, we zonally average the six energy conversion terms within the three regions shown in Fig. 2a. Strong positive KmKe is confined within the upper 400 m in the EAC jet and EAC eddy regions north of 36°S, except two small negative KmKe regions in the EAC upstream (Fig. 9a). One is between 24.5°S
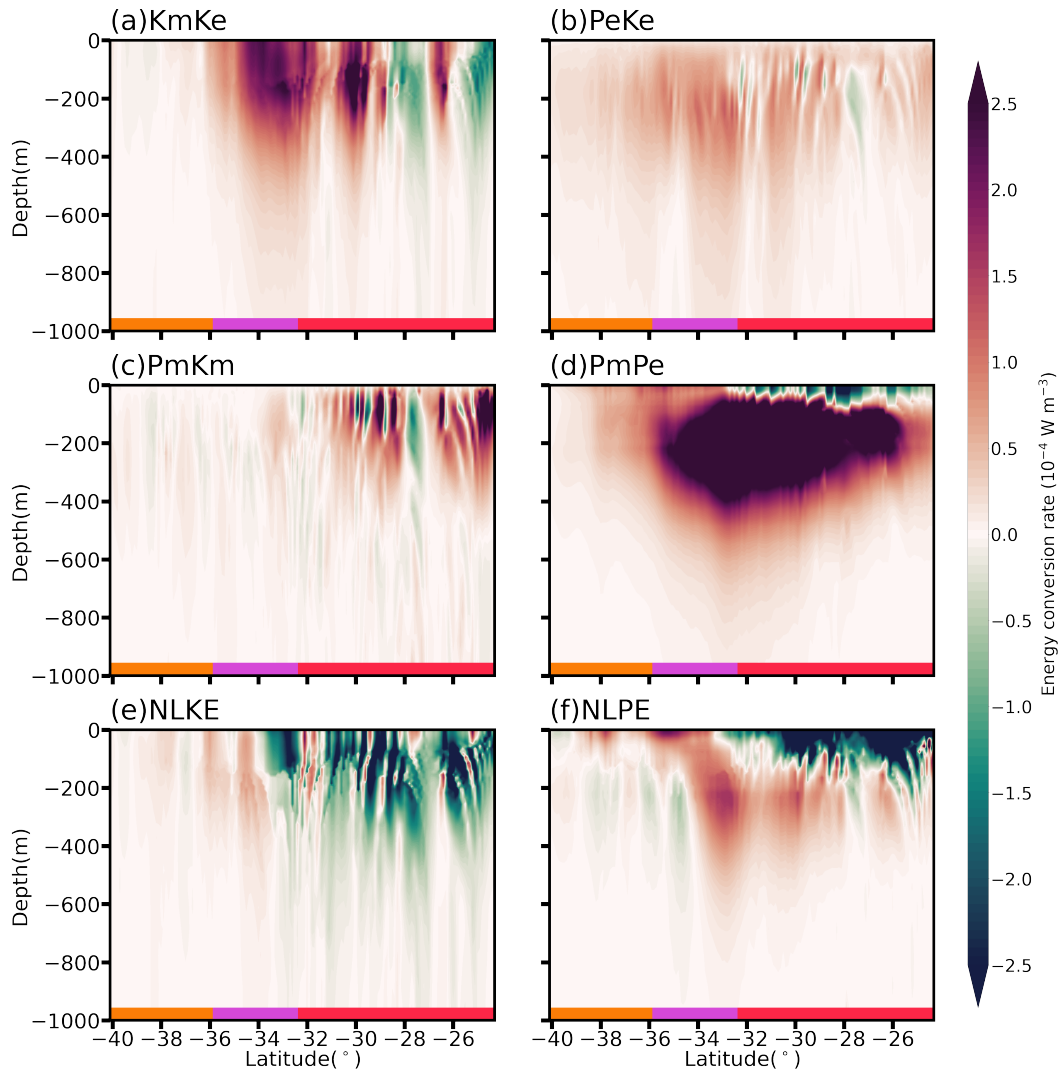
21

FIG. 9. Vertical profile (0-1000 m) of the zonal-mean (a) KmKe, (b) PeKe, (c) PmKm, (d) PmPe, (e) NLKE and (f) NLPE averaged between the 200 m isobath and 154.5°E along the EAC path. The thick red, purple and orange lines on the bottom of each panel indicate the EAC jet, EAC eddy and EAC southern extension regions, respectively, as shown in Fig. 2a.

and 26°S, and the other is between 27°S and 28.5°S. In contrast, PeKe is almost positive along the whole EAC path, but with a much weaker magnitude (Fig. 9b). This further demonstrates that barotropic instability is the main source of EKE in the EAC jet and EAC eddy regions.

In the EAC jet region, PmKm in the upper 400 m shows alternating positive–negative patterns north of 31°S (Fig. 9c). The available potential energy conversion (PmPe) of MPE↔EPE within the depth of 50 m - 400 m exhibits positive values between 26°S and 36°S (Fig. 9d), which is the

22

strongest among all energy conversion terms. In the top surface layer (< 50 m), however, we also find an inverse energy conversion from EPE to MPE north of 32°S (negative PmPe).

The energy conversion profiles of available potential energy and kinetic energy between the mean flow and the eddy field due to nonlocal eddy-mean flow interactions have different patterns along the EAC path. North of 34°S, strong negative NLKE dominates the upper 400 m (Fig. 9e). However, the NLKE in the upper 300 m is positive between 34°S and 36°S. This suggests nonlocal eddy-mean flow interactions transfer EKE in other regions to MKE north of 34°S. However, south of 34°S, the energy conversion is from MKE to remote EKE through nonlocal eddy-mean flow interactions. In the EAC upstream, we can find strong negative NLPE in the upper 150 m north of 32°S (Fig. 9f), with weak positive values in the subsurface (150 m - 400 m). In the EAC eddy region, strong positive NLPE dominates the upper 400 m, implying an inverse available potential energy conversion of EPE→MPE between 32°S and 36°S.
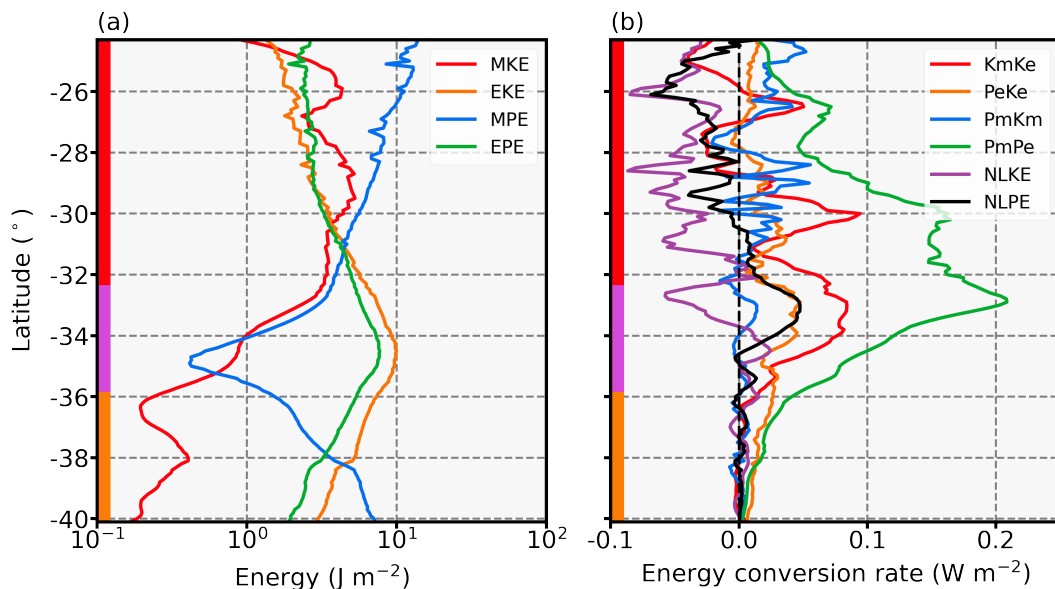

Fig. 10. Meridional distribution of the depth-integrated (0-1000 m) zonal-mean (a) energy reservoirs and (b) energy conversion terms averaged between the 200 m isobath and 154.5°E along the EAC path. The thick red, purple and orange lines on the left of each panel indicate the EAC jet, EAC eddy and EAC southern extension regions, respectively, as shown in Fig. 2a.

We further examine four energy reservoirs and six energy conversion terms integrated over the upper 1000 m along the EAC path. In the EAC jet region, the kinetic energy and available potential

energy in the mean flow are much larger than those in the eddy field between 24°S and 31°S, with MPE the largest among four energy reservoirs (Fig. 10a). In the EAC eddy and extension region, the EKE and EPE are much larger than MKE and MPE, with the EKE dominant between 32°S and 38°S.

As shown in Fig. 10b, the depth-integrated energy conversion terms have similar meridional distributions to Fig. 9. KmKe is negative within the latitudes of 24.5°S-26°S and 27°S-28.5°S, but it is much larger than PeKe and is the main source of EKE between 29°S and 35°S. PeKe is positive and weak along the EAC path, but it is larger than KmKe and contributes to the eddy growth south of 35°S. PmKm is positive in most latitudes, indicating the energy conversion from available potential energy to kinetic energy in the mean flow. Among all the energy conversion terms, PmPe is positive and the largest almost in the whole EAC path. The energy conversion of kinetic energy due to nonlocal eddy-mean flow interactions is from MKE to EKE north of 34°S and from EKE to MKE between 34°S and 36.5°S. Additionally, nonlocal eddy-mean flow interactions also contribute to the energy conversion of available potential energy from MPE to EPE north of 31.5°S and from EPE to MPE between 31.5°S and 34.5°S.

c. Energy budget

In this section, we show the eddy–mean flow energy budgets by examining the volume-integrated energy reservoirs and energy conversion terms in three subdomains along the EAC path (Fig. 11). More energy is contained in available potential energy than kinetic energy in the EAC jet region (Fig. 11b). The largest energy reservoir is MPE (6.06 PJ), followed by the EPE (2.68 PJ), MKE (2.42 PJ) and EKE (2.28 PJ), respectively. The ratio of MKE to MPE is 40% in the mean flow, but EKE and EPE is comparable in the eddy field with a ratio of 85% (EKE/EPE). The energy conversion rate of EKE through barotropic instability (MKE→EKE) is 1.31 GW. The baroclinic instability provides another indirect energy conversion pathway for EKE: MPE→EPE→EKE. Although the energy conversion rate from MPE to EPE is large (7.03 GW), eddies release less energy from available potential energy to kinetic energy with a transfer rate of 1.17 GW from EPE to EKE, which is smaller than that from MKE to EKE. The ratio of baroclinic to barotropic contribution to EKE production (PeKe/KmKe) is 89% in this region. As the leading energy reservoir, the MPE is the energy source, which also transfers energy to MKE with a rate of 1.27 GW and to EPE in other

24

regions with a rate of 0.81 GW. The mean flow also transfers MKE to EKE in the other regions with a rate of 2.41 GW through nonlocal eddy-mean flow interactions.

In the EAC eddy region (Fig. 11c), the eddy fields contain much larger kinetic energy and available potential energy than the mean flow. The ratio of MKE to EKE and MPE to EPE are only 13% and 20%, respectively. EKE (8.58 PJ) is much larger than EPE (6.78 PJ), MPE (1.36 PJ) and MKE (1.09 PJ). The ratio of PeKe to KmKe is 64%, implying that barotropic instability dominates the EKE production in this region, with an energy conversion rate of 5.22 GW from MKE to EKE. Similar to that in the EAC jet region, the baroclinic conversion of MPE→EPE→EKE also contributes to EKE production. However, the energy gain rate of EKE from EPE (3.33 GW) is only about one-third of that from MPE to EPE (11.08 GW). The mean flow can release part of its available potential energy to the kinetic energy, with a MPE→MKE conversion rate of 0.32 GW. Nonlocal eddy-mean flow interactions convert a small amount (0.08 GW) of MKE to EKE in other regions but contribute to the inverse energy conversion of EPE→MPE with a rate of 1.90 GW.

The energy reservoir in the eddy field is also very large in the EAC southern extension region (Fig. 11d). EKE (9.58 PJ) is the leading energy reservoir, followed by the MPE (8.90 PJ), EPE (6.69 PJ) and MKE (0.53 PJ), respectively. The ratio of MKE to EKE drops to 6%, but the ratio of MPE to EPE increases up to 133%. The energy conversion rate of MKE→EKE through barotropic instability decreases dramatically to 0.25 GW. In contrast, the energy conversion rate of EPE→EKE grows to 2.91 GW, implying that baroclinic instability dominates the EKE production in the EAC southern extension region. Compared to the EAC jet and EAC eddy region, the MPE→EPE conversion rate of 3.14 GW is relatively smaller. Similarly, the energy conversion rate of MPE→MKE is also small, with a value of 0.21 GW. Nonlocal eddy-mean flow interactions provide inverse energy conversion pathways of EKE→MKE and EPE→MPE, with conversion rates of 0.47 GW and 0.26 GW, respectively.

d. Synthesis

In the horizontal, strong MKE is confined within a narrow band between 24.5°S and 32.5°S in the main core of the EAC, while high EKE and EPE dominate the EAC eddy and EAC southern extension regions. We show that eddies drain energy from the mean flow to grow through two pathways: MKE→EKE and MPE→EPE→EKE. Strong barotropic instability dominates the EKE
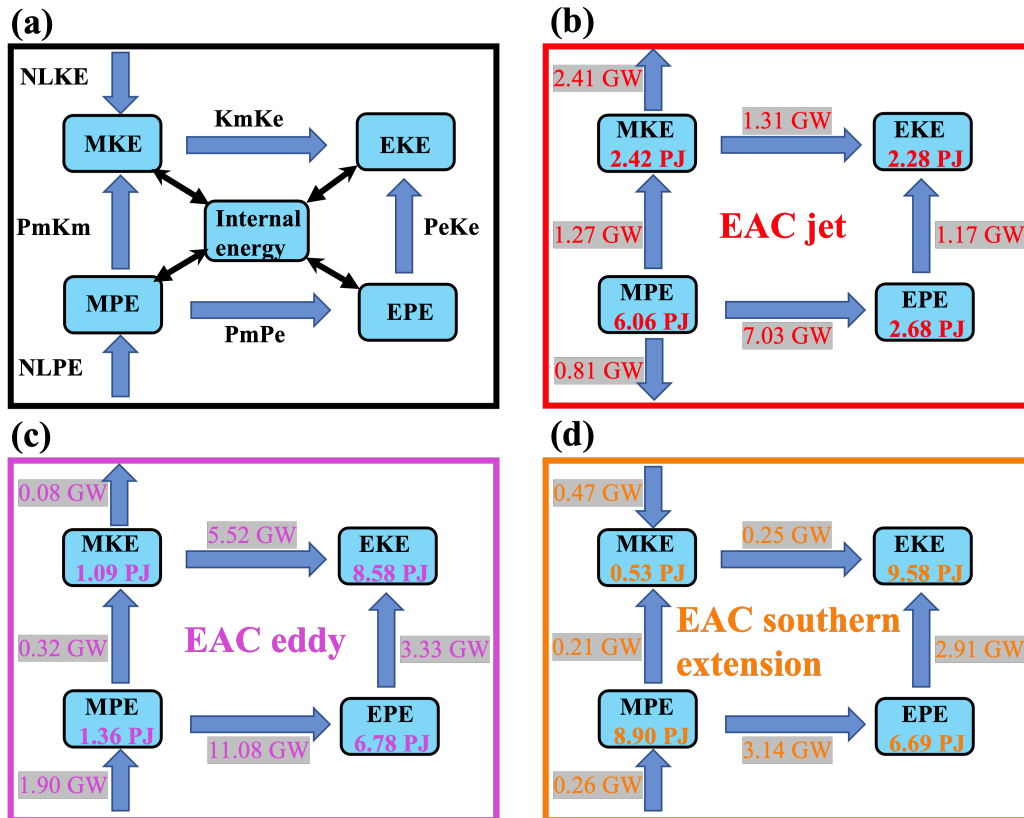
FIG. 11. Schematics of the volume-integrated eddy–mean flow energy budget in the upper 1000 m layer over the three subdomains indicated in Fig. 2a. Energy reservoirs are in units of petajoules (PJ = 10^{15}J) and energy conversion terms are in units of gigawatts (GW = 10^9W). The definition of each term is shown in panel a. Arrows represent the corresponding energy transfer direction.

production in the EAC jet and EAC eddy regions north of 36°S, while baroclinic instability dominates the EKE production in the EAC southern extension. Negative KmKe is also found in two small regions (24.5°S-26°S and 27°S-28.5°S), implying inverse energy conversion of kinetic energy from the eddy field to the mean flow. PmPe is the largest among the six energy conversion terms, indicating strong energy conversion from MPE to EPE through baroclinic instability between 29°S and 35.5°S. Nonlocal eddy-mean flow interactions also play a role in the energy conversion between the mean flow and the eddy fields. NLKE exhibits negative values along the EAC path from 24°S to 36°S, indicating the energy conversion from MKE to EKE in other regions. Positive NLKE is also found within two narrow bands south of 32°S in the inshore of the negative NLKE

band and the EAC return flow regions. The strong nonlocal available potential energy conversion is confined within the EAC upstream (north of 27°S) and the EAC eddy region.

In the vertical, the energy is mainly stored in the upper 500 m. The MKE and EKE keep the same horizontal structures with their strength decreasing dramatically with depth. However, the strongest EPE is confined within the upper 75 m along the whole EAC path, with another peak in the subsurface layer (155 m - 325 m) in the EAC eddy region. Overall, the horizontal distributions of the kinetic energy conversions MKE↔EKE (KmKe and NLKE) and MPE→MKE (PmKm) have similar patterns over the whole water column, but their magnitudes decrease with depth. Strong positive PmKm is confined within the top 300 m north of 32°S. The energy conversion of EPE→EKE (PeKe) also has a uniform horizontal structure but peaks in the subsurface layer, particularly between 100 m and 300 m in the EAC southern extension region. The horizontal structures of available potential energy conversions (PmPe and NLPE) between the mean flow and the eddy field (MPE↔EPE) vary with depths in the EAC jet region. Negative PmPe and NLPE dominate the surface 50 m and 150 m layer north of 32°S, respectively. Below the negative surface PmPe and NLPE, strong positive values extend deeper to 400 m. PmPe is the strongest below 50 m among six energy conversion terms, which peaks at around 217 m in the EAC jet and EAC eddy region but decreases with depth in the EAC southern extension.

Regions with large energy reservoirs correspond to strong energy conversions from the mean flow to the eddy field. In the horizontal, the EKE and EPE in the EAC eddy region are much stronger than the other regions (Figs. 2-3), with strong kinetic energy conversion (KmKe) and potential energy conversion (PmPe) from the mean flow to the eddy field in this region (Figs. 6-7). In the vertical, the EKE is constrained within the upper 450 m (Fig. 5b), where the KmKe is also stronger than the lower layers (Fig. 9a), and the EPE peaks in the subsurface layer (155 m - 325 m) within the strong PmPe depth of 50 m - 400 m (Fig. 9d).

For the volume-integrated energy reservoir and energy conversions, the energy is mainly stored in available potential energy instead of kinetic energy in the EAC jet region. The ratio of MKE/MPE and EKE/EPE is 40% and 85%, respectively. The energy conversion rate of MKE→EKE through barotropic instability is 1.31 GW, which is larger than the baroclinic instability conversion (EPE→EKE) of 1.17 GW. In the EAC eddy region, most energy is contained in the eddy fields instead of the mean flow. The ratio of MKE/EKE and MPE/EPE is 13% and 20%, respec-

tively. The barotropic instability dominates the EKE production, with an energy conversion rate of 5.22 GW from MKE to EKE. Similarly, the energy reservoir in the eddy field is also very large in the EAC southern extension region, with EKE the leading energy reservoir (9.58 PJ). The ratio of MKE to EKE drops to 6%, and the energy conversion rate of MKE→EKE decreases to 0.25 GW. In contrast, baroclinic instability is the primary source of EKE, with an energy conversion rate of 2.91 GW from EPE to EKE. The energy conversion between kinetic energy and available potential energy in the EAC system has similar magnitudes with that in the Kuroshio and Ryukyu Current regions (Yan et al. 2019, 2022).

5. Discussion

This study is the first to systematically investigate the detailed spatial structure of the eddy-mean flow interactions and energy budget along the EAC path on the basis of an eddy-resolving long-term (1998-2021) model simulation. Following the existing theoretical framework (KC15; Chen et al. 2014), we examined the three-dimensional structures of four energy reservoirs (MKE, EKE, MPE and EPE) and six energy conversion terms (KmKe, PeKe, PmKm, PmPe, NLKE and NLPE). Then, we present the characteristics of the eddy-mean flow energy distributions and conversions within three chosen subdomains (EAC jet, EAC eddy and EAC southern extension). We find that both local and nonlocal eddy-mean flow interactions exist in the EAC system, with inhomogeneous horizontal distributions.

While we have presented the first systematic eddy-mean flow study in the EAC, our results are in broad agreement with previous studies in the other WBCs. The energy reservoirs and conversion rates have complex horizontal and vertical structures, but with the same order of magnitude as those in the Gulf Stream (KC15) and Kuroshio and Ryukyu Currents (Yan et al. 2019). For example, the barotropic conversion is the main source of EKE in the EAC jet and EAC eddy regions, whereas baroclinic conversion dominates the EKE production in the EAC southern extension region. The double peak structure in the EPE profile has also been shown in the Kuroshio Current and Ryukyu Current regions (Yan et al. 2019) as well as the Gulf of Mexico (Maslo et al. 2020). We note our methodology is potentially more robust than that used in the Brazil Current where the density is assumed to be a function of the temperature only (Magalhães et al. 2017; Brum et al. 2017). It is known that the EAC is weaker but more eddying, with a high ratio of EKE/MKE east of the main

jet. The high EKE in the EAC system is comparable with that in the other WBCs, further study is needed to investigate the EKE variability in five major WBCs in the global ocean.

Our results, using a $0.1° \times 0.1°$ model BRAN2020, show spatial distributions of kinetic energy components (MKE and EKE). The spatial distribution of MKE is also consistent with satellite observations in Figs. 1a-b, which is a better representation than that of the lower resolution climate model used by Bull et al. (2020), implying that eddy-resolving resolution ($0.1°$) is needed to represent the EAC well. Additionally, our identified EKE sources (KmKe and PeKe) are mainly in agreement with results from a high-resolution regional modelling study (Li et al. 2021, 2022b) who looked at extreme events. Compared to previous results obtained from coarser horizontal resolution studies (Bowen et al. 2005; Mata et al. 2006; Bull et al. 2017), our eddy-resolving model simulation provides a more realistic representation of the EAC and associated mesoscale processes, allowing us to better understand the eddy-mean flow interactions in the EAC. We suggest that eddy-resolving resolution (< 10 km) is required to better represent mesoscale variability in the WBCs and improve our understanding of eddy-mean flow interactions.

In this study, we chose to use a data assimilating model BRAN2020 as our validation showed that it did a good job of representing the MKE and EKE variability in the system. Although the model fields in BRAN2020 are more realistic than OFAM2017 (a free running model) due to assimilation of surface data, we acknowledge that it also has some limitations. For example, because of the possible uncertainties introduced by assimilating observations, the momentum or mass is not conserved. However, the comparisons between BRAN2020 and OFAM2017 show that the spatial distributions of energy reservoirs and energy conversion terms are similar (e.g. Fig. 2). This gives us confidence that assimilating observations in BRAN2020 may have less impact on the results in this study. We also recognise that data assimilating models have been used for similar studies previously, e.g. Yang and Liang (2018, 2019). Additionally, spatial averaging within our three key dynamic regions has the disadvantage that the size of each box influences the magnitude of the values averaged within the box. However, within each box, the relative relationships between terms hold true. This issue is not unique to our study, and normalising by box size has not been done in other studies (e.g. KC15 and Yan et al. 2019).

Our study extends our knowledge of the three-dimensional structures of energy reservoirs and energy conversions in the EAC region and refines the results of recent studies on the eddy-mean flow

29

interactions in the WBCs. Consistent with regional model simulations (Li et al. 2021, 2022b), we demonstrate that barotropic instability is the primary source of EKE in the EAC jet and EAC eddy regions, but baroclinic instability dominates the EKE production in the EAC southern extension region. However, the results presented here only show the climatological characteristics of the eddy-mean flow interactions. To investigate the interactions between individual mesoscale eddies and the WBCs, such as eddy shedding (Marchesiello and Middleton 2000; Mata et al. 2006; Macdonald et al. 2016; Bull et al. 2017) or the impinging of mesoscale eddies on the WBCs (Li et al. 2020; Yan et al. 2022), we need a time-dependent eddy-mean energy framework. Chen et al. (2016) introduced a time-dependent energy diagram for eddy–mean flow interactions, which has been used to investigate the interactions between westward propagating mesoscale eddies and the Kuroshio Current by Yan et al. (2022) and will provide insights into eddy shedding and interactions in future EAC studies.

As suggested by Zhai et al. (2010), the western boundary acts as a 'graveyard' for the westward-propagating mesoscale eddies and provides a significant ocean eddy-energy sink in the global ocean. Over most of the EAC system, roughly 88% of mesoscale eddies propagate westward (Pilo et al. 2015). In the EAC upstream, it has been shown that a cyclonic-anticyclonic eddy pair propagated westward to reach and re-merge with the EAC between 24°S and 28°S (Li et al. 2020). Future work could examine the individual eddy shedding and the interaction between individual westward propagating mesoscale eddies and the EAC based on an energy analysis framework used in Yan et al. (2022).

Oceanic kinetic energy is dominated by the geostrophic eddy field (Ferrari and Wunsch 2009), and WBCs are hotspots of mesoscale eddies (Martínez-Moreno et al. 2021) and global warming (Wu et al. 2012). In a warming climate, WBCs are shifting poleward (Yang et al. 2016, 2020) and transporting more mass and warm water into the high-latitude regions. This will increase the barotropic and baroclinic instability in the WBC extensions, resulting in increased eddy shedding and ocean warming, as shown in the EAC southern extension (Li et al. 2022b). Eddy-rich regions are becoming more eddying during the past decades (Martínez-Moreno et al. 2021). Investigating the trends of EKE sources from barotropic (KmKe) and baroclinic (PeKe) instability is crucial for understanding the dynamics of increasing EKE and ocean warming in the WBC extensions. This

present work lays the foundation for us to now investigate the variability and trends in the WBCs as per (Li et al. 2022a).

31

Data availability statement. The BRAN2020 reanalysis and OFAM2017 model output are provided by CSIRO Australia and can be downloaded from `https://research.csiro.au/bluelink/outputs/data-access/` and `https://dapds00.nci.org.au/thredds/catalog/gb6/OFAM3/catalog.html`. The satellite altimetry products from Archiving, Validation and Interpretation of Satellite Oceanographic (AVISO) were produced by Ssalto/Duacs and distributed by EU Copernicus Marine and Environment Monitoring Service and are available at `https://resources.marine.copernicus.eu/product-detail/SEALEVEL_GLO_PHY_L4_MY_008_047`.

References

Bowen, M. M., J. L. Wilkin, and W. J. Emery, 2005: Variability and forcing of the East Australian Current. *J. Geophys. Res. Oceans*, **110**, C03 019, https://doi.org/10.1029/2004JC002533.

Brum, A. L., J. L. L. de Azevedo, L. R. de Oliveira, and P. H. R. Calil, 2017: Energetics of the Brazil Current in the Rio Grande Cone region. *Deep-Sea Res. I: Oceanogr. Res. Pap.*, **128**, 67–81, https://doi.org/10.1016/j.dsr.2017.08.014.

Bull, C. Y., A. E. Kiss, A. S. Gupta, N. C. Jourdain, D. Argüeso, A. D. Luca, and G. Sérazin, 2020: Regional Versus Remote Atmosphere-Ocean Drivers of the Rapid Projected Intensification of the East Australian Current. *J. Geophys. Res. Oceans*, **125**, e2019JC015 889, https://doi.org/10.1029/2019JC015889.

Bull, C. Y., A. E. Kiss, N. C. Jourdain, M. H. England, and E. van Sebille, 2017: Wind Forced Variability in Eddy Formation, Eddy Shedding, and the Separation of the East Australian Current. *J. Geophys. Res. Oceans*, **122**, 9980–9998, https://doi.org/10.1002/2017JC013311.

32

Bull, C. Y. S., A. E. Kiss, E. van Sebille, N. C. Jourdain, and M. H. England, 2018: The Role of the New Zealand Plateau in the Tasman Sea Circulation and Separation of the East Australian Current. *J. Geophys. Res. Oceans*, **123**, 1457–1470, https://doi.org/10.1002/2017JC013412.

Cetina-Heredia, P., M. Roughan, E. V. Sebille, and M. A. Coleman, 2014: Long-term trends in the East Australian Current separation latitude and eddy driven transport. *J. Geophys. Res. Oceans*, **119**, 4351–4366, https://doi.org/10.1002/2014JC010071.

Chamberlain, M. A., P. R. Oke, R. A. S. Fiedler, H. M. Beggs, G. B. Brassington, and P. Divakaran, 2021: Next generation of Bluelink ocean reanalysis with multiscale data assimilation: BRAN2020. *Earth Syst. Sci. Data*, **13**, 5663–5688, https://doi.org/10.5194/essd-13-5663-2021.

Chen, R., G. R. Flierl, and C. Wunsch, 2014: A Description of Local and Nonlocal Eddy–Mean Flow Interaction in a Global Eddy-Permitting State Estimate. *J. Phys. Oceanogr.*, **44**, 2336–2352, https://doi.org/10.1175/JPO-D-14-0009.1.

Chen, R., A. F. Thompson, and G. R. Flierl, 2016: Time-Dependent Eddy-Mean Energy Diagrams and Their Application to the Ocean. *J. Phys. Oceanogr.*, **46**, 2827–2850, https://doi.org/10.1175/JPO-D-16-0012.1.

Ducet, N., P. Y. Le Traon, and G. Reverdin, 2000: Global high-resolution mapping of ocean circulation from TOPEX/Poseidon and ERS-1 and -2. *J. Geophys. Res. Oceans*, **105**, 19 477–19 498, https://doi.org/10.1029/2000JC900063.

Everett, J. D., M. E. Baird, P. R. Oke, and I. M. Suthers, 2012: An avenue of eddies: Quantifying the biophysical properties of mesoscale eddies in the Tasman Sea. *Geophys. Res. Lett.*, **39**, L16 608, https://doi.org/10.1029/2012GL053091.

Feng, M., X. Zhang, P. Oke, D. Monselesan, M. Chamberlain, R. Matear, and A. Schiller, 2016: Invigorating ocean boundary current systems around Australia during 1979–2014: As simulated in a near-global eddy-resolving ocean model. *J. Geophys. Res. Oceans*, **121**, 3395–3408, https://doi.org/10.1002/2016JC011842.

Ferrari, R., and C. Wunsch, 2009: Ocean Circulation Kinetic Energy: Reservoirs, Sources, and Sinks. *Annu. Rev. Fluid Mech.*, **41**, 253–282, https://doi.org/10.1146/annurev.fluid.40.111406.102139.

Godfrey, J. S., G. R. Cresswell, T. J. Golding, A. F. Pearce, and R. Boyd, 1980: The Separation of the East Australian Current. *J. Phys. Oceanogr.*, **10**, 430–440, https://doi.org/10.1175/1520-0485(1980)010<0430:TSOTEA>2.0.CO;2.

Gula, J., M. J. Molemaker, and J. C. McWilliams, 2015: Gulf Stream Dynamics along the Southeastern U.S. Seaboard. *J. Phys. Oceanogr.*, **45**, 690–715, https://doi.org/10.1175/JPO-D-14-0154.1.

Halo, I., P. Penven, B. Backeberg, I. Ansorge, F. Shillington, and R. Roman, 2014: Mesoscale eddy variability in the southern extension of the East Madagascar Current: Seasonal cycle, energy conversion terms, and eddy mean properties. *J. Geophys. Res. Oceans*, **119**, 7324–7356, https://doi.org/10.1002/2014JC009820.

Hu, D., and Coauthors, 2015: Pacific western boundary currents and their roles in climate. *Nature*, **522**, 299–308, https://doi.org/10.1038/nature14504.

Kang, D., and E. N. Curchitser, 2015: Energetics of Eddy–Mean Flow Interactions in the Gulf Stream Region. *J. Phys. Oceanogr.*, **45**, 1103–1120, https://doi.org/10.1175/JPO-D-14-0200.1.

Kerry, C., and M. Roughan, 2020: Downstream Evolution of the East Australian Current System: Mean Flow, Seasonal, and Intra-annual Variability. *J. Geophys. Res. Oceans*, **125**, e2019JC015 227, https://doi.org/10.1029/2019JC015227.

Kuo, Y.-C., and C.-S. Chern, 2011: Numerical study on the interactions between a mesoscale eddy and a western boundary current. *J. Oceanogr.*, **67**, 263–272, https://doi.org/10.1007/s10872-011-0026-3.

Li, J., M. Roughan, and C. Kerry, 2021: Dynamics of Interannual Eddy Kinetic Energy Modulations in a Western Boundary Current. *Geophys. Res. Lett.*, **48**, e2021GL094 115, https://doi.org/10.1029/2021GL094115.

Li, J., M. Roughan, and C. Kerry, 2022a: Drivers of ocean warming in the western boundary currents of the Southern Hemisphere. *Nat. Clim. Chang.*, **12**, 901–909, https://doi.org/10.1038/s41558-022-01473-8.

34

Li, J., M. Roughan, and C. Kerry, 2022b: Variability and Drivers of Ocean Temperature Extremes in a Warming Western Boundary Current. *J. Clim.*, **35**, 1097–1111, https://doi.org/10.1175/JCLI-D-21-0622.1.

Li, Z., X. Wang, J. Hu, F. P. Andutta, and Z. Liu, 2020: A Study on an Anticyclonic-Cyclonic Eddy Pair Off Fraser Island, Australia. *Front. Mar. Sci*, **7**, 594 358, https://doi.org/10.3389/fmars.2020.594358.

Macdonald, H. S., M. Roughan, M. E. Baird, and J. Wilkin, 2016: The formation of a cold-core eddy in the East Australian Current. *Cont. Shelf Res.*, **114**, 72–84, https://doi.org/10.1016/j.csr.2016.01.002.

Magalhães, F. C., J. L. Azevedo, and L. R. Oliveira, 2017: Energetics of eddy-mean flow interactions in the Brazil current between 20°S and 36°S. *J. Geophys. Res. Oceans*, **122**, 6129–6146, https://doi.org/10.1002/2016JC012609.

Marchesiello, P., and J. H. Middleton, 2000: Modeling the East Australian Current in the Western Tasman Sea. *J. Phys. Oceanogr.*, **30**, 2956–2971, https://doi.org/10.1175/1520-0485(2001)031<2956:MTEACI>2.0.CO;2.

Martínez-Moreno, J., A. M. Hogg, M. H. England, N. C. Constantinou, A. E. Kiss, and A. K. Morrison, 2021: Global changes in oceanic mesoscale currents over the satellite altimetry record. *Nat. Clim. Chang.*, **11**, 397–403, https://doi.org/10.1038/s41558-021-01006-9.

Maslo, A., J. M. A. C. de Souza, and J. S. Pardo, 2020: Energetics of the Deep Gulf of Mexico. *J. Phys. Oceanogr.*, **50**, 1655–1675, https://doi.org/10.1175/JPO-D-19-0308.1.

Mata, M. M., S. E. Wijffels, J. A. Church, and M. Tomczak, 2006: Eddy shedding and energy conversions in the East Australian Current. *J. Geophys. Res. Oceans*, **111**, C09 034, https://doi.org/10.1029/2006JC003592.

Nilsson, C. S., and G. R. Cresswell, 1980: The formation and evolution of East Australian current warm-core eddies. *Prog. Oceanogr.*, **9**, 133–183, https://doi.org/10.1016/0079-6611(80)90008-7.

35

Oke, P. R., and J. H. Middleton, 2000: Topographically Induced Upwelling off Eastern Australia. *J. Phys. Oceanogr.*, **30**, 512–531, https://doi.org/10.1175/1520-0485(2000)030<0512:TIUOEA>2.0.CO;2.

Oke, P. R., G. S. Pilo, K. Ridgway, A. Kiss, and T. Rykova, 2019a: A search for the Tasman Front. *J. Mar. Syst.*, **199**, 103 217, https://doi.org/10.1016/j.jmarsys.2019.103217.

Oke, P. R., and Coauthors, 2013: Evaluation of a near-global eddy-resolving ocean model. *Geosci. Model Dev.*, **6**, 591–615, https://doi.org/10.5194/gmd-6-591-2013.

Oke, P. R., and Coauthors, 2019b: Revisiting the circulation of the East Australian Current: Its path, separation, and eddy field. *Phys. Oceanogr.*, **176**, 102 139, https://doi.org/10.1016/j.pocean.2019.102139.

Pilo, G. S., M. M. Mata, and J. L. L. Azevedo, 2015: Eddy surface properties and propagation at Southern Hemisphere western boundary current systems. *Ocean Sci.*, **11**, 629–641, https://doi.org/10.5194/os-11-629-2015.

Ridgway, K., and J. Dunn, 2003: Mesoscale structure of the mean East Australian Current System and its relationship with topography. *Prog. Oceanogr.*, **56**, 189–222, https://doi.org/10.1016/S0079-6611(03)00004-1.

Sloyan, B. M., and T. J. O'Kane, 2015: Drivers of decadal variability in the Tasman Sea. *J. Geophys. Res. Oceans*, **120**, 3193–3210, https://doi.org/10.1002/2014JC010550.

Sloyan, B. M., K. R. Ridgway, and R. Cowley, 2016: The East Australian Current and Property Transport at 27°S from 2012 to 2013. *J. Phys. Oceanogr.*, **46**, 993–1008, https://doi.org/10.1175/JPO-D-15-0052.1.

Storch, J. S. V., C. Eden, I. Fast, H. Haak, D. Hernández-Deckers, E. Maier-Reimer, J. Marotzke, and D. Stammer, 2012: An Estimate of the Lorenz Energy Cycle for the World Ocean Based on the 1/10° STORM/NCEP Simulation. *J. Phys. Oceanogr.*, **42**, 2185–2205, https://doi.org/10.1175/JPO-D-12-079.1.

Tedesco, P., J. Gula, P. Penven, and C. Ménesguen, 2022: Mesoscale Eddy Kinetic Energy Budgets and Transfers between Vertical Modes in the Agulhas Current. *J. Phys. Oceanogr.*, **52**, 677–704, https://doi.org/10.1175/JPO-D-21-0110.1.

Tilburg, C. E., H. E. Hurlburt, J. J. O'Brien, and J. F. Shriver, 2001: The Dynamics of the East Australian Current System: The Tasman Front, the East Auckland Current, and the East Cape Current. *J. Phys. Oceanogr.*, **31**, 2917–2943, https://doi.org/10.1175/1520-0485(2001)031<2917:TDOTEA>2.0.CO;2.

Vallis, G. K., 2017: *Atmospheric and Oceanic Fluid Dynamics: Fundamentals and Large-Scale Circulation*. 2nd ed., Cambridge University Press, 335–378 pp.

Witter, D. L., and D. B. Chelton, 1998: Eddy–Mean Flow Interaction in Zonal Oceanic Jet Flow along Zonal Ridge Topography. *J. Phys. Oceanogr.*, **28**, 2019–2039, https://doi.org/10.1175/1520-0485(1998)028<2019:EMFIIZ>2.0.CO;2.

Wu, L., and Coauthors, 2012: Enhanced warming over the global subtropical western boundary currents. *Nat. Clim. Change*, **2**, 161–166, https://doi.org/10.1038/nclimate1353.

Yan, X., D. Kang, E. N. Curchitser, and C. Pang, 2019: Energetics of Eddy–Mean Flow Interactions along the Western Boundary Currents in the North Pacific. *J. Phys. Oceanogr.*, **49**, 789–810, https://doi.org/10.1175/JPO-D-18-0201.1.

Yan, X., D. Kang, C. Pang, L. Zhang, and H. Liu, 2022: Energetics Analysis of the Eddy–Kuroshio Interaction East of Taiwan. *J. Phys. Oceanogr.*, **52**, 647–664, https://doi.org/10.1175/JPO-D-21-0198.1.

Yang, H., G. Lohmann, W. Wei, M. Dima, M. Ionita, and J. Liu, 2016: Intensification and poleward shift of subtropical western boundary currents in a warming climate. *J. Geophys. Res. Oceans*, **121**, 4928–4945, https://doi.org/10.1002/2015JC011513.

Yang, H., and Coauthors, 2020: Poleward Shift of the Major Ocean Gyres Detected in a Warming Climate. *Geophys. Res. Lett.*, **47**, e2019GL085 868, https://doi.org/10.1029/2019GL085868.

Yang, Y., and X. S. Liang, 2016: The Instabilities and Multiscale Energetics Underlying the Mean–Interannual–Eddy Interactions in the Kuroshio Extension Region. *J. Phys. Oceanogr.*, **46**, 1477–1494, https://doi.org/10.1175/JPO-D-15-0226.1.

Yang, Y., and X. S. Liang, 2018: On the Seasonal Eddy Variability in the Kuroshio Extension. *J. Phys. Oceanogr.*, **48**, 1675–1689, https://doi.org/10.1175/JPO-D-18-0058.1.

Yang, Y., and X. S. Liang, 2019: New perspectives on the generation and maintenance of the kuroshio large meander. *J. Phys. Oceanogr.*, **49**, 2095–2113, https://doi.org/10.1175/JPO-D-18-0276.1.

Zhai, X., H. L. Johnson, and D. P. Marshall, 2010: Significant sink of ocean-eddy energy near western boundaries. *Nat. Geosci.*, **3**, 608–612, https://doi.org/10.1038/ngeo943.